The Astrophysical Journal, 890:85 (14pp), 2020 February 10 https://doi.org/10.3847/1538-4357/ab6b21

Dissecting the Phase Space Snail Shell

Zhao-Yu Li[1,2,3] and Juntai Shen[1,2,3,4]
[1] Department of Astronomy, School of Physics and Astronomy, Shanghai Jiao Tong University, 800 Dongchuan Road, Shanghai 200240, People's Republic of China
lizy.astro@sjtu.edu.cn, jtshen@sjtu.edu.cn
[2] Shanghai Key Laboratory for Particle Physics and Cosmology, 200240, Shanghai, People's Republic of China
[3] Shanghai Astronomical Observatory, Chinese Academy of Sciences, 80 Nandan Road, Shanghai 200030, People's Republic of China
[4] College of Astronomy and Space Sciences, University of Chinese Academy of Sciences, 19A Yuquan Road, Beijing 100049, People's Republic of China
Received 2019 September 12; revised 2019 December 2; accepted 2020 January 12; published 2020 February 14

Abstract

The ongoing vertical phase-mixing, manifesting itself as a snail shell in the $Z - V_Z$ phase space, has been discovered with *Gaia* DR2 data. To better understand the origin and properties of the phase-mixing process, we study the vertical phase-mixing signatures in arches (including the classical "moving groups") of the $V_R - V_\phi$ phase space near the solar circle. Interestingly, the phase space snail shell exists only in the arches with $|V_\phi - V_{\rm LSR}| \lesssim 30\,{\rm km\,s^{-1}}$, i.e., stars on dynamically "colder" orbits. The snail shell becomes much weaker and eventually disappears for increasingly larger radial action (J_R), quantifying the "hotness" of orbits. Thus, one should pay closer attention to the colder orbits in future phase-mixing studies. We also confirm that the Hercules stream has two branches (at fast and slow V_ϕ), which may not be explained by a single mechanism, since only the fast branch shows the prominent snail shell feature. The hotter orbits may have phase-wrapped away already due to the much larger dynamical range in radial variation to facilitate faster phase-mixing. To explain the lack of a well-defined snail shell in the hotter orbits, the disk should have been perturbed at least 500 Myr ago. Our results offer more support to the recent satellite-disk encounter scenario than the internal bar-buckling perturbation scenario as the origin of the phase space mixing. The origin of the more prominent snail shell in the V_ϕ color-coded phase space is also discussed.

Unified Astronomy Thesaurus concepts: Milky Way dynamics (1051); Milky Way disk (1050); Galaxy structure (622); Galaxy disks (589)

1. Introduction

The Milky Way disk is not in complete dynamical equilibrium. It shows a prominent structure in kinematic space that is phase-mixing in both the horizontal and vertical directions. Since full phase space information for individual stars is obtainable, the Milky Way is uniquely equipped to reveal disk dynamical evolution in detail. The picture of the Milky Way's evolution is complicated because it is affected by both internal and external perturbations. The resonances of the bar and spiral arms can significantly influence the stellar orbits to cause radial migration in the disk (Friedli et al. 1994; Sellwood & Binney 2002; Roškar et al. 2008; Minchev & Famaey 2010) and to generate substructures in the velocity phase space for stars in the solar neighborhood (Dehnen 2000; Fux 2001; Antoja et al. 2009; Antoja et al. 2011; Quillen et al. 2011; Hunt & Bovy 2018). Large-scale bulk motions observed in the Galactic disk (e.g., Siebert et al. 2011; Carlin et al. 2013; Sun et al. 2015; Tian et al. 2017; Wang et al. 2018a, 2018b) can also be induced from dynamical processes related to the bar and spiral arms (Siebert et al. 2012; Debattista 2014; Faure et al. 2014; Monari et al. 2015, 2016). Moreover, satellite galaxies or sub-halos interacting with the Milky Way can perturb the disk to generate warps, flares, or other vertical motions such as the bending and breathing features in the outer disk (Hunter & Toomre 1969; Quinn et al. 1993; Kazantzidis et al. 2008; Purcell et al. 2011; Gómez et al. 2013; Widrow et al. 2014; D'Onghia et al. 2016; Laporte et al. 2018a, 2018b).

Using revolutionary *Gaia* data Antoja et al. (2018) discovered clear evidence of vertical phase-mixing in the solar neighborhood for the first time. A clear snail shell can be seen in the $Z - V_Z$ phase space. As first shown in Laporte et al. (2019), the phase space snail shell is also prominent in the number density contrast map. This feature can be understood as the phase-mixing process in a vertically perturbed disk, where the vertical oscillation frequency depends on the oscillation amplitude, generating a snail shell structure in $Z - V_Z$ space (Tremaine 1999; Antoja et al. 2018). Candlish et al. (2014) investigated the evolution of the phase-mixing process for disrupting star clusters that show development and winding of a phase space spiral due to the anharmonic oscillation.[5] In fact, the concept of phase-mixing/wrapping has been implied in several previous works. Minchev et al. (2009) showed that an unrelaxed disk can produce wave-like features in the velocity phase space that get closer due to the phase wrapping. As shown in Quillen et al. (2009), external perturbations could excite phase-mixing for stars in the disk to induce streams in the velocity distribution. de la Vega et al. (2015) found that phase wrapping excited by external perturbations might account for the bending and breathing modes in the disk. The north/south asymmetry in the vertical stellar number density profile discovered in Widrow et al. (2012) is also a reflection of the snail shell, with all the stars projected on the Z axis.

The phase space snail shell shows up more clearly when color-coded with the azimuthal velocity (V_ϕ) of stars (Figure 1(c) in Antoja et al. 2018), which was suggested to indicate the tight correlation between the in-plane and vertical motions. The two motions are clearly entangled, but there are still important details to be clarified (Binney & Schönrich 2018; Darling & Widrow 2019). Laporte et al. (2019) found snail shells at different stellar age bins, and the shape of the snail changes

[5] See Figure 4.27 in Binney & Tremaine (2008) for a schematic view of the phase-mixing process.

systematically across the Galactic disk. Similar results are also obtained in other studies (Tian et al. 2018; Wang et al. 2019). One possible culprit for the vertical perturbation is the merging of the Sagittarius dwarf with the last pericentric passage that occurred at ∼300–900 Myr ago (Antoja et al. 2018; Binney & Schönrich 2018; Bland-Hawthorn et al. 2019; Laporte et al. 2019). A competing scenario is spontaneous bending waves as a source of long-lived internal vertical perturbers (Chequers & Widrow 2017), which includes the perturbation from a bar-buckling event (Khoperskov et al. 2019).

It is well known that the velocity phase space in the solar neighborhood, e.g., $V_R - V_\phi$, shows complex kinematic substructures, known as "moving groups" (Dehnen 1998; Skuljan et al. 1999; Famaey et al. 2005; Antoja et al. 2008). *Gaia* revealed new configurations in phase space: the multiple arches in the $V_R - V_\phi$ space and diagonal ridges in the $R - V_\phi$ space (Antoja et al. 2018; Gaia Collaboration et al. 2018b). The arches appear for the whole range of azimuthal velocity, with all the classical moving groups embedded in the more extended arched substructures (Gaia Collaboration et al. 2018b). Ramos et al. (2018) remarked that the more roundish moving groups and the elongated arches are morphologically different entities, with some moving groups belonging to the same arch. To the first order, the velocity phase space can be considered an assembly of arches. Previous studies argued that the internal dynamical effects of structures in the Galactic disk mainly generate kinematic features with radial velocity (U) and azimuthal velocity (V) with respect to the local circular motion within $\sim$50 km s^{-1} (Minchev et al. 2009). On the other hand, stars with larger radial and azimuthal velocities resembling arc-like features in the $U - V$ plane may be related to the disk-ringing effect caused by external interactions with satellite galaxies (Minchev et al. 2009; Gómez et al. 2012).

Considering the different internal or external origins of the arches, the connection between the arches and previous vertical perturbation events is still an open question. For example, Michtchenko et al. (2019) reported that the snail shell is only produced by the classical moving groups, with no evidence of incomplete vertical phase-mixing from external perturbations. This apparent inconsistency with other works needs to be explored by properly dissecting the velocity phase space into distinct arches. Here we utilize the radial velocity, proper motions, and parallax information from the second *Gaia* data release (DR2) to investigate the properties of different arches in the $Z - V_Z$ phase space. Hopefully, this study will shed light on the origin of the snail shell and the correlation between the in-plane and vertical motions. The sample is described in Section 2. The results are shown and discussed in Section 3, and summarized in Section 4.

2. Sample

2.1. Sample Selection

Gaia DR2 launches a new era of precise stellar dynamics, providing astrometric parameters for 1.3 billion sources down to $G \sim 21$ mag, as well as line-of-sight velocities for 7.2 million stars brighter than 12 mag, with the median parallax uncertainty for bright sources ($G < 14$ mag) at 0.03 mas and the proper motion uncertainty at 0.07 mas yr^{-1} (Gaia Collaboration et al. 2018a). We adopted the same sample selection criteria as Antoja et al. (2018), i.e., selecting stars with positive parallaxes ϖ with relative uncertainty less than 20% ($\varpi/\sigma_\varpi > 5$). As pointed out by Antoja et al. (2018), the sample selection makes $1/\varpi$ a reasonably good distance estimator (Schönrich & Aumer 2017; Luri et al. 2018).

The sample consists of 6.2 million stars, covering the region with $4 < R < 13$ kpc. Following Antoja et al. (2018), we adopt $(X_\odot, Y_\odot, Z_\odot) = (-8.34, 0, 0.027)$ kpc as the Sun position (Reid et al. 2014). The local standard of rest (LSR) circular velocity $V_{\rm LSR}$ is set to 240 km s^{-1} (Reid et al. 2014). Here we adopt the peculiar velocities of the Sun with respect to LSR as $(U_\odot, V_\odot, W_\odot) = (11.1, 12.24, 7.25)$ km s^{-1} (Schönrich 2012). Our main results are not affected if we choose other measurements of the solar peculiar motion, e.g., Tian et al. (2015) or Huang et al. (2015). The typical velocity uncertainty is about 1 km s^{-1} for the radial, azimuthal, and vertical velocities (Antoja et al. 2018; Gaia Collaboration et al. 2018a).

In this study, we select the stars in a narrow annulus in the solar neighborhood ($R = 8.34 \pm 0.1$ kpc), which contains ∼0.93 million stars. The $V_R - V_\phi$ phase space distribution of stars in the solar neighborhood is known to show a variety of arches and clumps. The positions of the major arches are consistent with recent works (Antoja et al. 2018; Gaia Collaboration et al. 2018b; Ramos et al. 2018). We confirm that the stars in this sample show the same snail shells in the $Z - V_Z$ phase space when color-coded with the number density, V_R, and V_ϕ, as in Antoja et al. (2018).

To evaluate the influence of the parallax bias in the *Gaia* catalog, we also tested our results with the parallax-corrected *Gaia* sample (Schönrich et al. 2019). The parallax-corrected sample size is reduced to 60% of that used here. The snail shell patterns in both samples are in excellent agreement; our results and main conclusions are unaffected by the parallax correction, since most of the stars are still very close to the solar neighborhood.

2.2. Identification of Arches

We further dissect the sample in the $V_R - V_\phi$ phase space into different arches containing the classical moving groups, e.g., Sirius, Hyades, Coma Berenices (hereafter Coma for brevity), Pleiades, and Hercules. By applying the Stationary Wavelet Transform (Starck & Murtagh 2002) on the $V_R - V_\phi$ distribution of *Gaia* DR2 data in the solar neighborhood, Ramos et al. (2018) identified 12 arches (A1 to A12). Adopting the positions and extensions of the arches in Ramos et al. (2018), we dissect the velocity phase space into different regions corresponding to these 12 arches.

We identify the gaps between these arches by adjusting the contrast level of the number density map (see the Appendix for more information). Figure 1 shows the arches separated by the dotted lines in the velocity phase space. Clearly, the arches are well separated.[6] The classical moving groups, such as Sirius, Coma, and Hyades–Pleiades, are embedded in arches A4, A5, and A7, respectively. Note that arches A8 and A9 together form the Hercules stream (Gaia Collaboration et al. 2018b; Ramos et al. 2018). Considering their azimuthal velocity difference, we refer to A8 as the Hercules Fast branch with median $V_\phi \sim 209$ km s^{-1}, and A9 as the Hercules Slow branch with median $V_\phi \sim 202$ km s^{-1}. The properties of the arches are listed in Table 1. V_Z is not considered when classifying arches.

[6] Arches A10 and A11 are grouped together due to the ambient boundary between them.

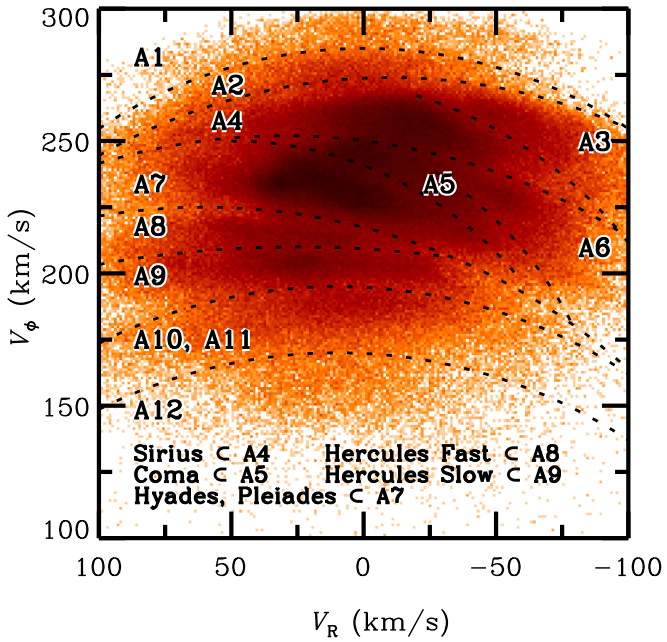

Figure 1. $V_R - V_\phi$ phase space of the sample around $R = 8.34$ kpc. Arches are separated with dotted lines. Table 1 also lists the classical moving groups and the corresponding arches that they belong to.

To highlight the snail shell in the number density map of the $Z - V_Z$ phase space, we adopt the method in Laporte et al. (2019) to derive the number density contrast ΔN,

$$\Delta N = \frac{N}{\widetilde{N}} - 1, \quad (1)$$

where $\widetilde{N}$ is the Gaussian kernel convolved number density distribution.

To further increase the visibility of the snail shell, we generate the enhanced map based on the ΔN map. Since the intershell region in the ΔN map has values typically less than -0.03, we can significantly enhance the snail shell pattern by showing only those regions with $\Delta N \geqslant -0.03$.

3. Results and Discussion

3.1. Dissecting the Phase Space Snail Shell

The $Z - V_Z$ phase space distributions of the arches are shown in Figures 2–4, which are color-coded with number density N, number density contrast ΔN, enhanced map, radial velocity V_R, and azimuthal velocity V_ϕ. The arches are grouped according to the prominence of the phase space snail shell. The arches with prominent snail shells are shown in Figure 2, arches with moderate snail shells are shown in Figure 3, and arches with indistinct snail shells are shown in Figure 4.

In Figure 2, for each arch, the snail shells revealed in N, ΔN, and enhanced maps are almost identical. The snail shell pattern is slightly different in the V_R and V_ϕ color-coded phase space compared to the number density map, but the amplitude contrast of the snail shell is only 2–4 km s^{-1}. This may be due to the variation of the snail shell shape with the radial or azimuthal velocities for each arch, which will be discussed in greater detail in Section 3.5. For arch A8, there seems to be no visible snail shell in the V_R or V_ϕ color-coded phase space.

From the $V_R - V_\phi$ phase space in Figure 1, it seems that the snail shell only exists for arches with $210 \lesssim V_\phi \lesssim 270$ km s^{-1} (i.e., $|V_\phi - V_{\rm LSR}| \lesssim 30$ km s^{-1}). This velocity range corresponds to the dynamically colder orbits, which are closer to circular orbits. Stars with velocities outside that region are denoted hotter orbits.

We also quantify the amplitude/contrast of the snail shell. For the $Z - V_Z$ phase space distribution of each arch, along a constant Z slit, the ΔN profile as a function of V_Z is extracted. The Z slit range listed in Table 1 is purposely chosen to cut through the shell (local maximum) and intershell regions (local minimum). The profiles of the number density contrast are shown in Figure 5. The colder orbits (top panel) show large fluctuations with a similar zigzag pattern due to the multiple intersections of the snail shell with the slit, while the hotter orbits (middle panel) show roughly flat profiles with small fluctuations, indicating the weak or indistinct snail shell in the hotter orbits. To quantify the amplitude of the snail shell, in each profile, we measure the difference between the maximum value within $-30 < V_Z < -20$ km s^{-1} and the minimum value within $-20 < V_Z < 10$ km s^{-1}. The results are also listed in Table 1. Clearly, the amplitude/contrast of the snail shell in colder orbits ($\sim$0.3) is significantly higher than that of the hotter orbits ($\sim$0.03).

Figure 6 shows the phase space distributions for all the stars on colder orbits (top row; including A3, A4, A5, A6, A7, and A8) and hotter orbits (bottom row; including A1, A2, A9, A10, A11, and A12). Stars on the colder orbits clearly show a very prominent snail shell in the number density (left) and V_ϕ color-coded phase space (right), and a slightly weaker snail shell in the V_R color-coded phase space (middle). On the other hand, the hotter orbits (the bottom row) do not exhibit the clear snail shells in the number density, V_R or V_ϕ color-coded phase spaces. If the phase space snail shell really exists in the hotter orbits, it is significantly blurred or incoherent. The bottom panel in Figure 5 compares the density profiles between the combined colder and hotter orbits, confirming our argument for the prominent snail shell in the colder orbits only. Note that in Figure 6, for the colder orbits, the snail shell patterns between the ΔN and V_ϕ color-coded phase spaces are different. This probably indicates that the snail shell shape varies across the arches in the colder orbits. This will be discussed in greater detail in 3.5.

As shown in Figure 4, the phase space distributions of arches A10, A11, and A12 are more elongated along the V_Z axis than arches A1 and A2. This is consistent with simple theoretical expectations of approximately harmonic oscillators. The difference between the median azimuthal velocities of the arches at high and low V_ϕ is $\sim$100 km s^{-1}, corresponding to $\sim$3.5 kpc in terms of the difference in the guiding radius (R_g).[7] Therefore, compared to the arch at higher V_ϕ, stars with lower V_ϕ have much smaller R_g, where both the vertical oscillation frequency and vertical velocity amplitude are larger ($V_{Z,\,\rm max} \sim \Omega_z Z_{\rm max}$), resulting in a more elongated distribution along the vertical velocity axis in the $Z - V_Z$ phase space. This simple argument is also consistent with the snail shape variation found by Laporte et al. (2019) in their Figure 15 for a region centered on $R = 6$ kpc, which is more elongated along the V_Z axis compared to the snail shell at $R = 10$ kpc. Similar results are also seen in Wang et al. (2019).

One may use the radial action J_R to quantify the extent of the radial oscillation (or "hotness") of orbits. We use the action-based

[7] $R_g \approx \frac{V_\phi \times R_0}{V_c}$, assuming a flat rotation curve.

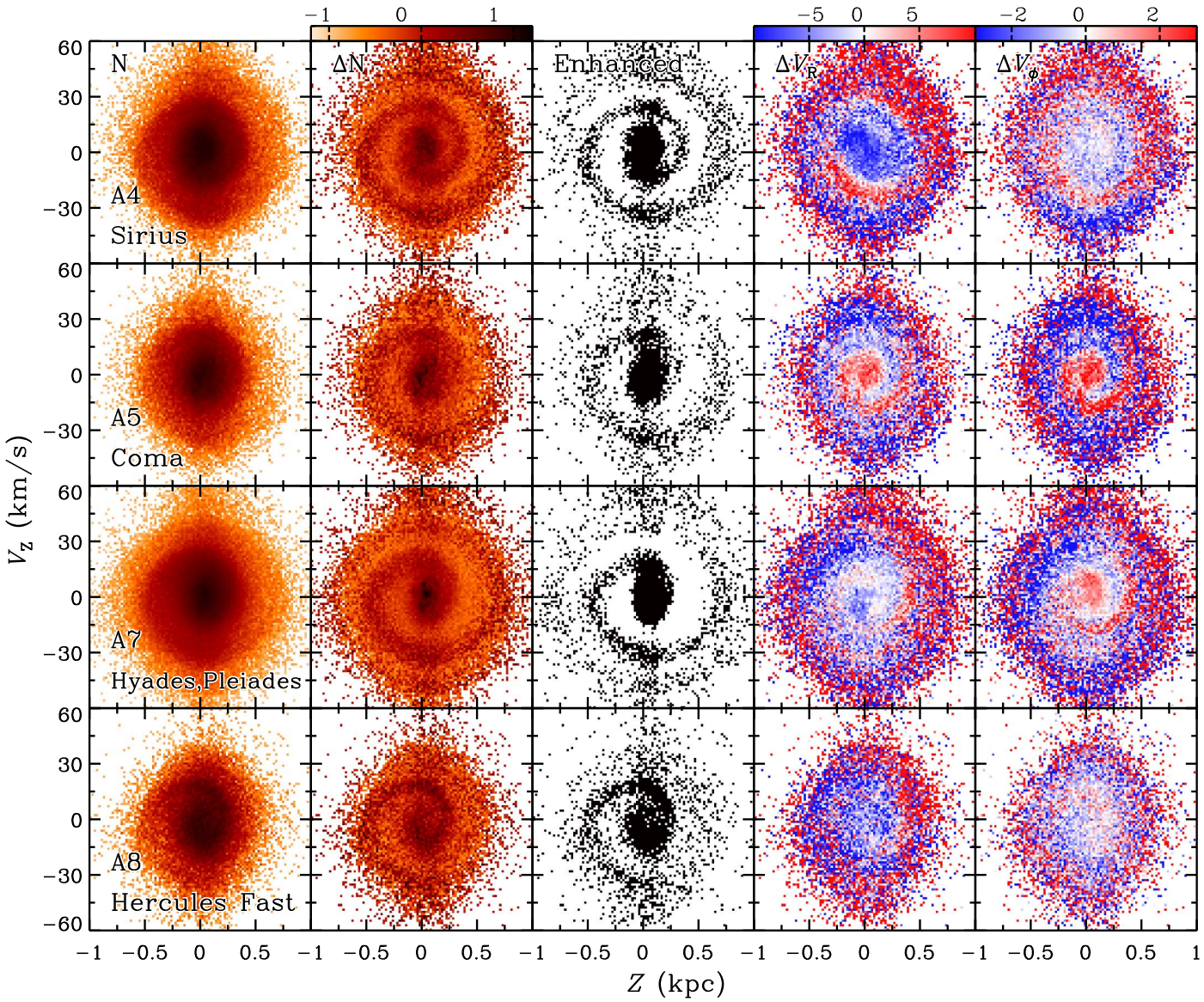

Figure 2. $Z - V_Z$ phase space of arches A4, A5, A7, and A8 showing a prominent snail shell pattern. From left to right, the columns correspond to the phase space distribution color-coded with number density N, number density contrast ΔN, density enhanced map, radial velocity V_R and azimuthal velocity V_ϕ, respectively. Each pixel corresponds to 0.02 kpc $\times$ 1.2 km s^{-1}. The Gaussian kernel width used to construct the density contrast map is empirically chosen as 14 pixels to best highlight the snail shell. Note that in the V_R and V_ϕ color-coded phase space, the median value has been subtracted.

galaxy modeling package AGAMA (Vasiliev 2019) to directly compute J_R of each star in our sample, with the best-fit potential from McMillan (2011) adopted. J_R has the dimension of angular momentum. Its unit in our paper is kpc^2 Myr^{-1}. Figure 7 shows the J_R color-coded $V_R - V_\phi$ phase space distribution of our sample. As expected, J_R is smaller for nearly circular orbits with velocities closer to the circular velocity of the LSR. Figure 8 shows the $Z - V_Z$ phase space distributions for stars in different J_R ranges. The snail shell becomes much weaker for increasingly larger J_R values; the snail shell is indistinct with $J_R > 0.04$. This phenomenon is expected since stars with large J_R occupy a wide range of guiding radius distribution, resulting in a significantly blurred snail shell. Moreover, hotter stars respond poorly to dynamical perturbations.

This could also explain why the snail shells of arches A3 and A6 shown in Figure 3 are not as prominent as those in Figure 2 (for A4, A5, A7, and A8). The stars in A3 and A6 have large radial action ($J_R > 0.04$) to blur the snail shell feature.

In Figure 7, the red ellipse represents the contour of $J_R = 0.04$, which agrees well with the azimuthal velocity ranges of colder orbits marked with the two black dashed lines. The $Z - V_Z$ phase space distributions of stars with $J_R < 0.04$ and $J_R > 0.04$ are shown in Figure 9. A clear snail shell can only be seen for the subsample with $J_R < 0.04$. The lower panels with $J_R > 0.04$ show a significantly blurred or incoherent snail shell feature. This agrees with Figure 6, confirming that hotter orbits (with larger radial oscillation) do not show prominent snail shells in phase space. Arches A3 and A6 are partially included in the sample with $J_R > 0.04$ to result in a blurred snail shell feature in the lower right panel of Figure 9 for the V_ϕ color-coded phase space.

The median J_R of our sample is 0.018, which is very similar to the result in Bland-Hawthorn et al. (2019) within a few percent ($\sim$0.0195 after being converted to our unit). The larger J_R subsample (above the median J_R) of Bland-Hawthorn et al. (2019) shows a weak phase space snail shell. Apparently, their

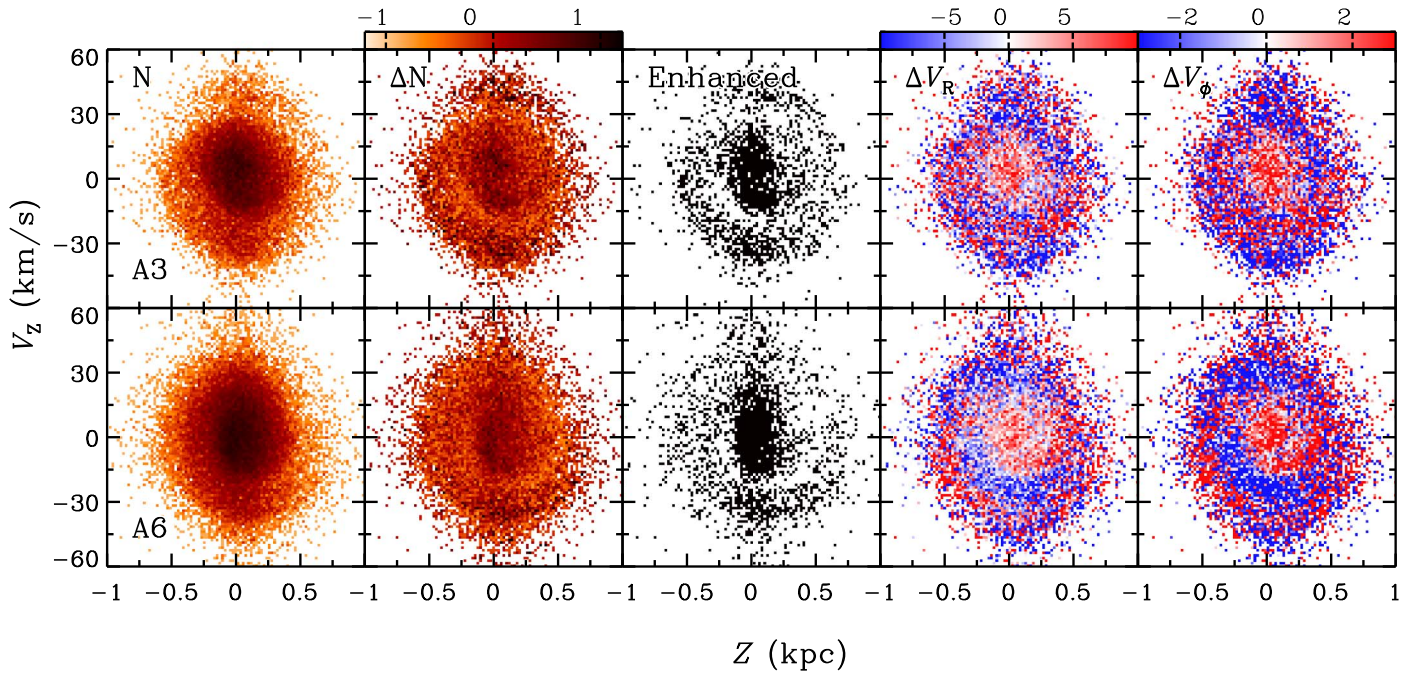

Figure 3. $Z - V_Z$ phase space of arches A3 and A6 showing a moderate snail shell feature. The layout mirrors that of Figure 2. The prominences of the snail shells are moderate here.

Table 1
Properties of the Arches in the $V_R - V_\phi$ Phase Space

Arch ID (1)	Contains (2)	Number of Stars (3)	Snail Amplitude (4)	Snail Prominence (5)	Range of Z slit (kpc) (6)
A1	⋯	8,966	0.086	Indistinct	[−0.34, −0.20]
A2	⋯	16,335	0.005	Indistinct	[−0.34, −0.20]
A3	γLeo	36,540	0.422	Moderate	[−0.32, −0.24]
A4	Sirius	183,689	0.332	Prominent	[−0.34, −0.28]
A5	Coma, Dehnen98−6	106,166	0.282	Prominent	[−0.30, −0.20]
A6	Dehnen98−14	61,412	0.186	Moderate	[−0.26, −0.18]
A7	Hyades, Pleiades	287,909	0.304	Prominent	[−0.26, −0.18]
A8	Hercules Fast	58,537	0.377	Prominent	[−0.34, −0.26]
A9	Hercules Slow, ϵInd	84,978	0.045	Indistinct	[−0.40, −0.28]
A10, A11	HR 1614, Bobylev16−22	49,909	0.027	Indistinct	[−0.40, −0.28]
A12	Arcturus	17,383	0.059	Indistinct	[−0.40, −0.28]

Note. Col. (1): arch ID adopted from Ramos et al. (2018). Col. (2): classical moving groups contained in the arch. Col. (3): number of stars in this arch. Col. (4): amplitude/contrast of the snail shell in each arch, which is defined as the difference between the local maximum and minimum values in the corresponding V_Z ranges of the ΔN profile along a narrow Z slit in the phase space. Col. (5): prominence of the phase space snail shell. Col. (6): the range of Z slit used to extract the ΔN profile for the snail shell amplitude calculation.

high J_R subsample contains a significant fraction of colder orbits defined by us, thus giving rise to the weak snail shell.

3.2. Two Branches of the Hercules Stream

The Hercules stream, as a prominent low azimuthal velocity structure in velocity phase space, has been extensively studied in the literature. Stellar spectra of individual stars in the stream suggest multiple stellar populations with different ages and metallicities, arguing against the stream as a disrupted stellar cluster or the debris of a satellite galaxy (Famaey et al. 2005; Bensby et al. 2007). Previous theoretical works have suggested that the Hercules stream is due to the dynamical effects of the bar and/or spiral arms (Dehnen 2000; Antoja et al. 2014; Pérez-Villegas et al. 2017; Hunt & Bovy 2018).

Gaia DR2 showed that the Hercules stream is composed of two branches at different azimuthal velocities (Gaia Collaboration et al. 2018b; Ramos et al. 2018). For the two branches of the Hercules stream, it is surprising to see that only the fast branch (arch A8; bottom row in Figure 2) shows the prominent snail shell but not for the slow branch (arch A9; middle row in Figure 4). This difference should be physical and not due to small number statistics, since the slow branch (A9) even has ∼40% more stars than the fast branch (A8) as listed in Table 1. Therefore, the Hercules stream may not be a homogeneous kinematic structure. If the two branches can be explained by a single mechanism, then it is difficult to understand the difference in the vertical phase space distributions, considering the small azimuthal velocity difference (∼7 km s^{-1}) between the two branches.

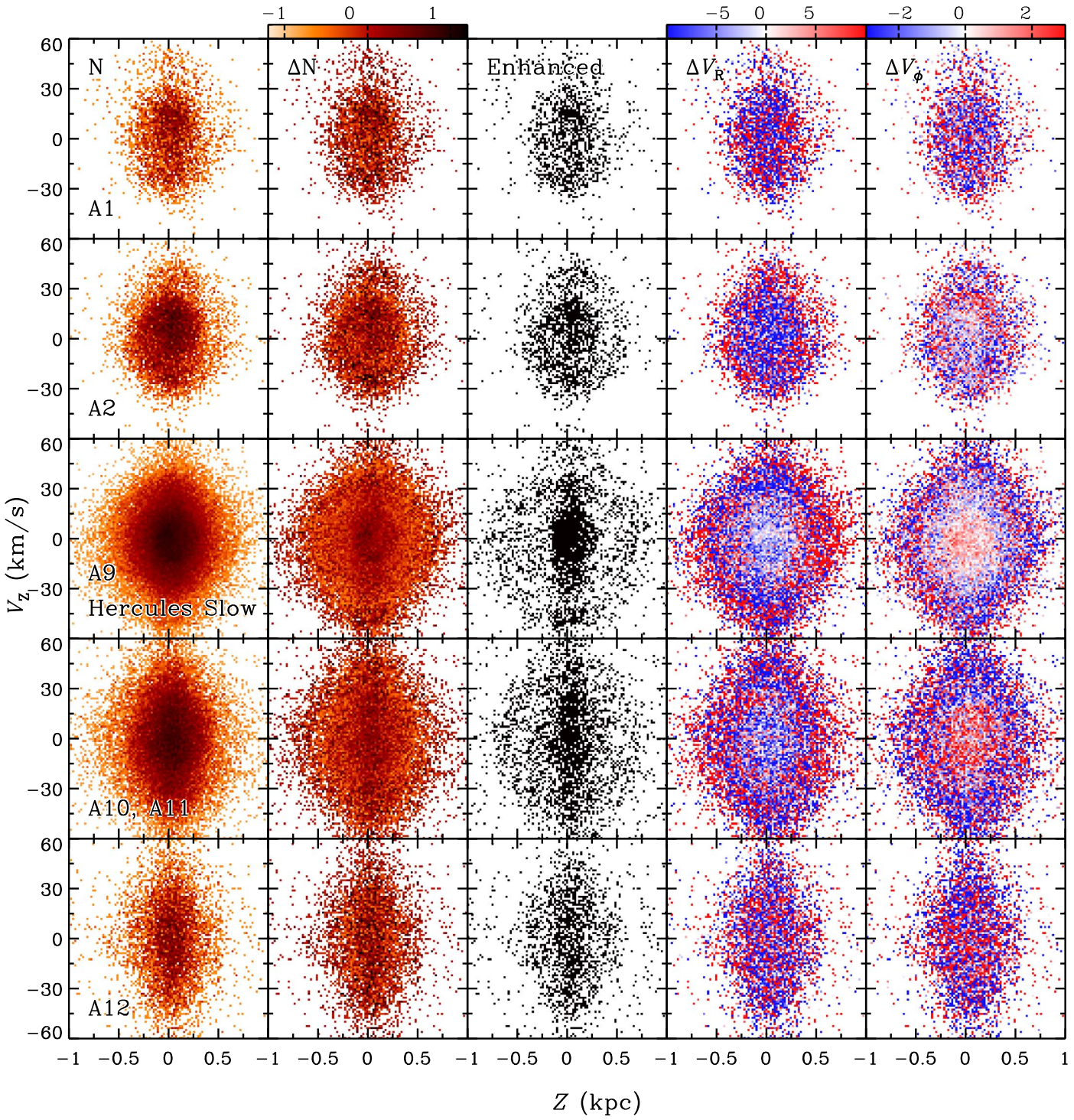

Figure 4. $Z - V_Z$ phase space of arches A1, A2, A9, A10, A11, and A12 showing a blurred or absent snail shell feature. The layout mirrors that of Figure 2. The snail shells here are indistinct compared to Figures 2 and 3.

3.3. Phase Mixing in Colder and Hotter Orbits

The snail shell in the $Z - V_Z$ phase space reflects the vertical phase-mixing with anharmonic oscillation (Antoja et al. 2018). Stars with larger vertical action J_Z have smaller vertical oscillation frequency Ω_Z (Binney & Schönrich 2018). Binney & Schönrich (2018) also showed that Ω_Z depends sensitively on V_ϕ, with smaller Ω_Z at larger V_ϕ, which forms a narrow and sequential distribution in the $\Omega_Z - \sqrt{J_Z}$ plane for each V_ϕ; the snail shell shape may change slightly at different V_ϕ. Our result shows clear phase space snail shells for stars in individual arches on the colder orbits. The snail shell shapes of these arches are also slightly different from each other, as shown in Figure 2. This is roughly consistent with Binney & Schönrich (2018); each arch usually has a small V_ϕ range, which corresponds nicely to a narrow strip in the $\Omega_Z - \sqrt{J_Z}$ plane to induce a clear phase space snail shell.

Binney & Schönrich (2018) suggested that the unclear snail shell in the phase space number density distribution observed

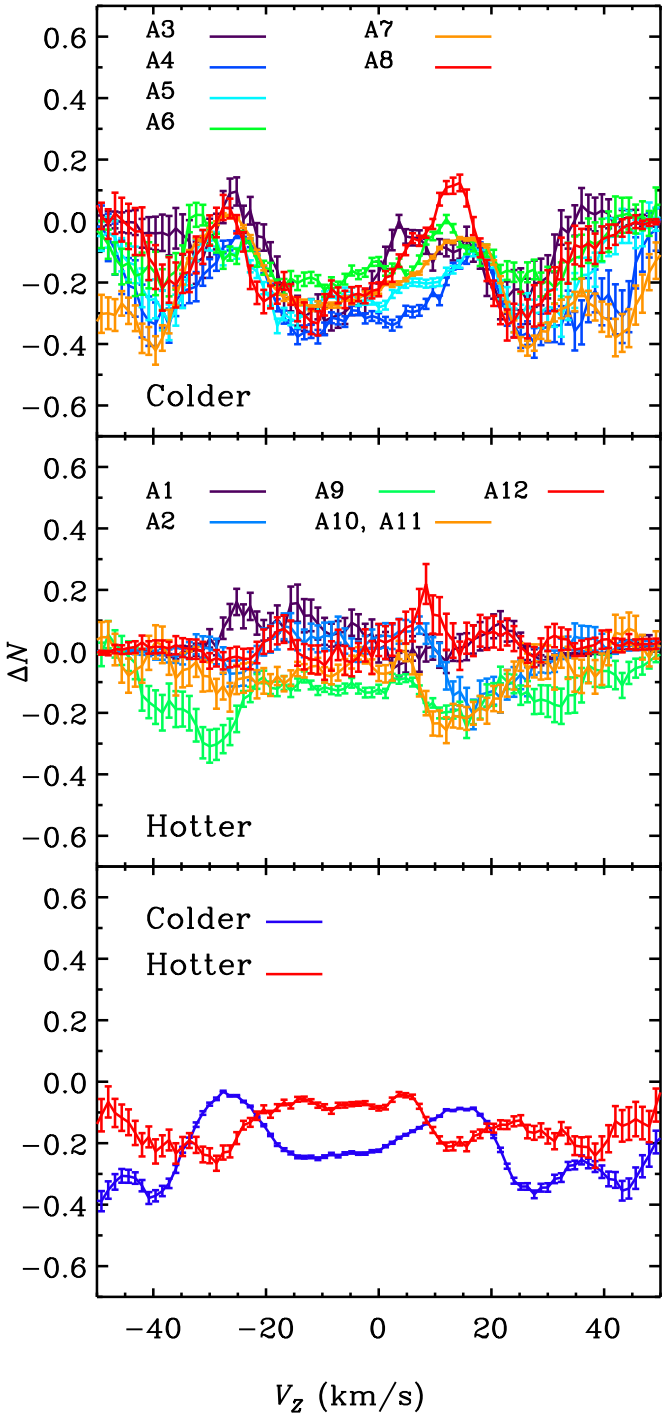

Figure 5. Snail shells amplitude quantification. Number density contrast profiles along a constant Z slit (see Table 1) for arches in the colder and hotter orbits are shown in the top and middle panels, respectively. The bottom panel compares the density profiles of all the stars on colder or hotter orbits; from the profiles, we use the difference between the local maximum within $-30 < V_Z < -20$ and the local minimum within $-20 < V_Z < 10$ to quantify the amplitude of the snail shell.

in Antoja et al. (2018) is due to the fact that stars lie in a "broad swath" in the $\Omega_Z - \sqrt{J_Z}$ plane. As shown in the top left panel of Figure 6, all the stars on colder orbits combined together show a prominent snail shell in the phase space number density distribution. These results may indicate that the distribution of stars on colder orbits in the $\Omega_Z - \sqrt{J_Z}$ plane is more well-defined and narrower than "a broad swath."

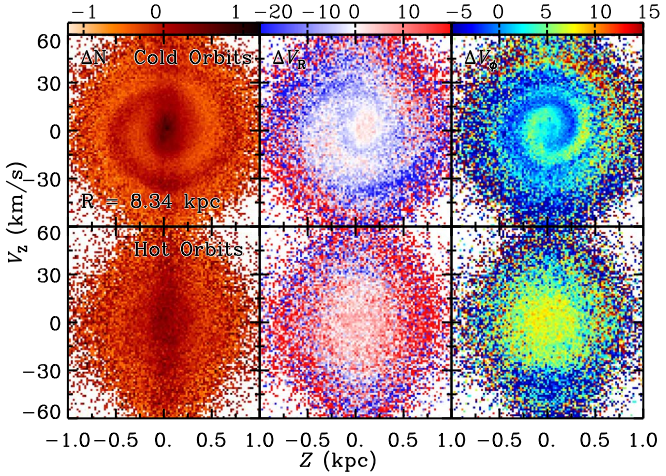

Figure 6. $Z - V_Z$ phase space of all the stars on the colder orbits (top row) and hotter orbits (bottom row). The colder orbits include arches A3, A4, A5, A6, A7, and A8, while the hotter orbits contain A1, A2, A9, A10, A11, and A12. The left, middle, and right columns show the phase space color-coded with ΔN, ΔV_R, and ΔV_ϕ, respectively.

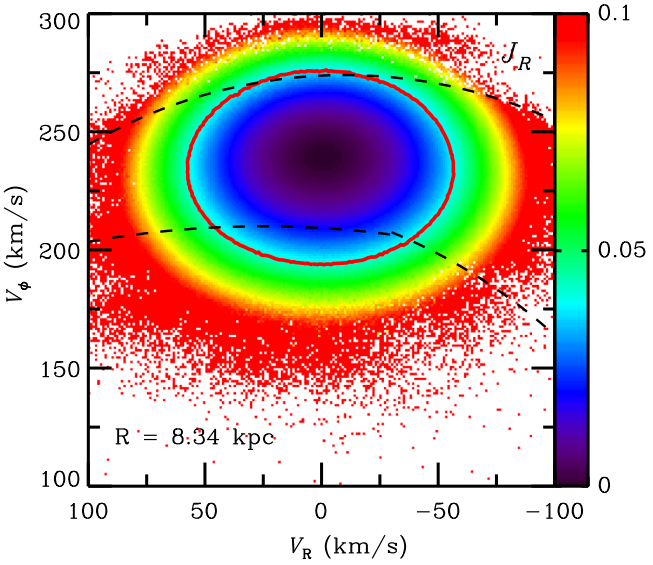

Figure 7. $V_R - V_\phi$ phase space distribution of our sample color-coded with J_R, which quantifies the extent of the radial oscillation. J_R has the dimension of the angular momentum in units of kpc^{2}Myr^{-1}. The red ellipse represents the contour at $J_R = 0.04$ to separate the colder and hotter orbits. The black dashed lines mark the boundaries in Figure 1 for the colder and hotter orbits. They are in agreement in terms of the range of V_ϕ.

Both the analytical estimation and simple test particle simulations using *galpy*[8] (Bovy 2015) with MWPotential2014 show that stars on hotter orbits typically have much larger dynamical ranges in the disk with radial oscillation amplitudes $(R_{\rm max} - R_{\rm min})/2 \sim 2$ kpc than stars on colder orbits ($\lesssim$0.7 kpc). It is therefore natural that hotter orbits will scramble the signal, as hotter stars arrive at this very local sample from a range of guiding radii. As shown in Bland-Hawthorn et al. (2019), given the same amplitude of the vertical perturbation, stars on circular orbits at larger radii will form a more loosely winding phase

[8] http://github.com/jobovy/galpy

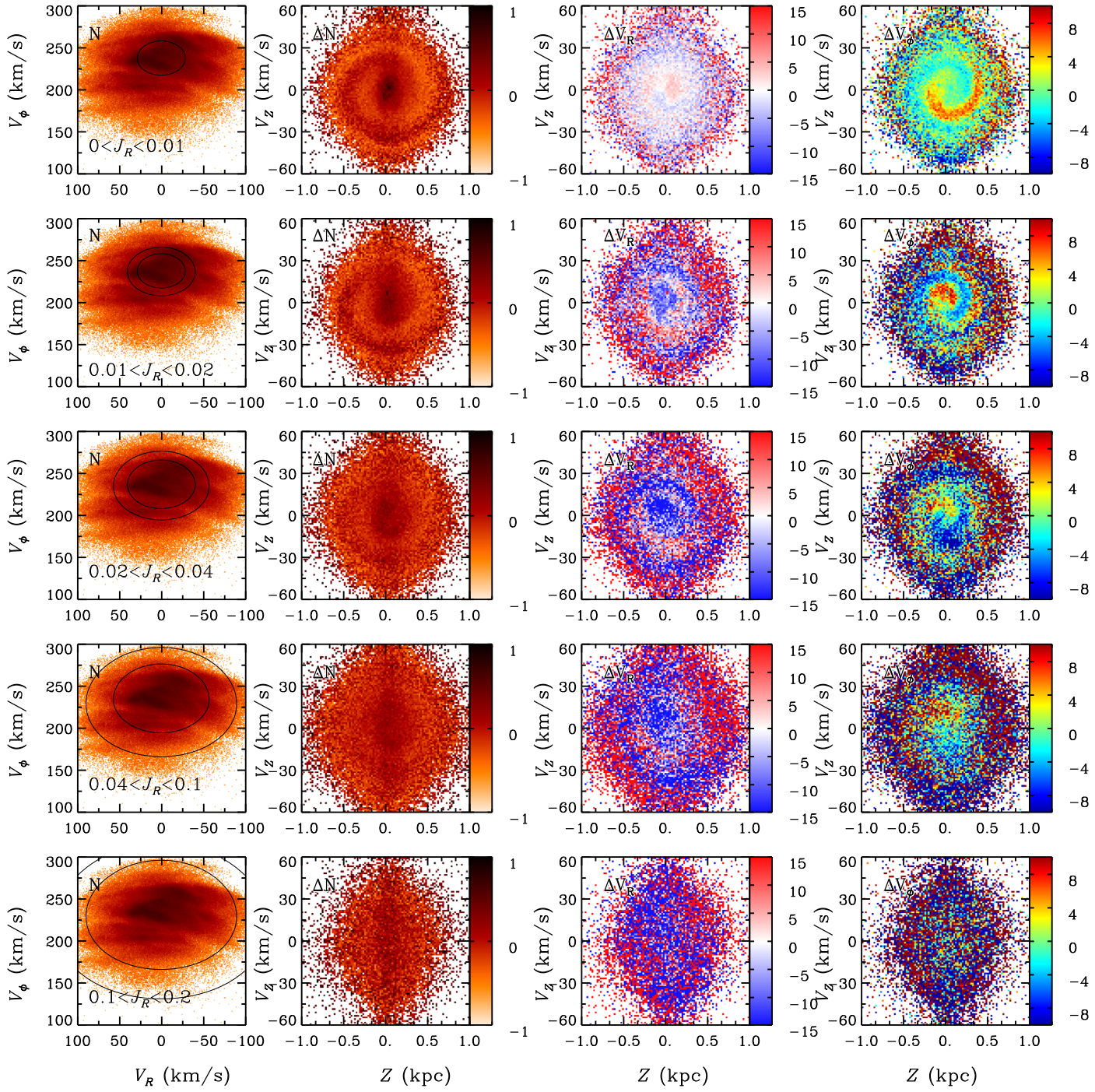

Figure 8. $Z - V_Z$ phase space distributions for stars in different J_R ranges. The left column shows the $V_R - V_\phi$ phase space of the whole sample overlaid with the ellipse contours of the lower and upper boundaries of the J_R ranges. For each J_R range, the second, third, and fourth columns represent the $Z - V_Z$ phase space distributions color-coded with ΔN, V_R, and V_ϕ, respectively. From top to bottom, the gradual disappearance of a snail shell in increasingly "hotter" (higher J_R) orbits is clear.

space snail shell at lower vertical oscillation frequency than the stars on circular orbits at smaller radius. The snail shell at larger radius becomes more elongated in the Z direction, but reduced in the V_Z direction ($\Omega_z \sim V_{Z,\max}/Z_{\max}$). Due to the large radial range of the hotter orbits, the elongation of the $Z - V_Z$ phase space ellipse changes during its radial oscillation, leading to a blurred distribution and faster phase-mixing.

Stars on hotter orbits have probably phase-wrapped away already to show a significantly blurred and indistinct snail shell, while the stars on the colder orbits are still in the process of vertical phase-mixing. To demonstrate this argument we perform a simple simulation with 100,000 test particles in a realistic Milky Way potential (Irrgang et al. 2013; Antoja et al. 2018) to track the evolution of the hotter and colder orbits. Note that our test particle simulation is designed to mimic an external vertical perturbation. We have verified that it can reproduce the simulation results in Antoja et al. (2018), e.g., their Figure 3(a) and extended Figures 3(a) and (b).

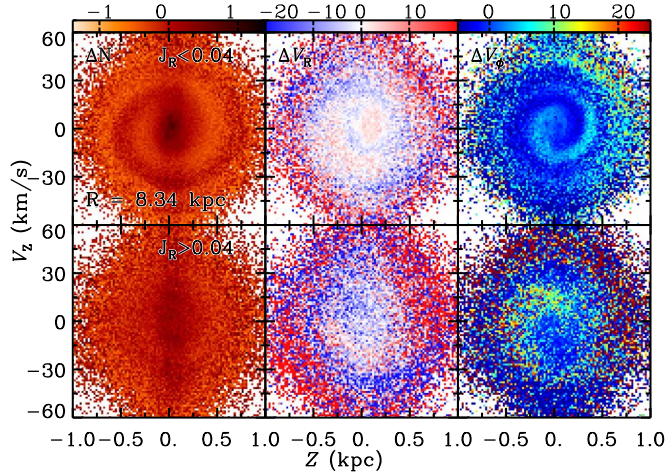

Figure 9. $Z - V_Z$ phase space distributions for the stars with $J_R < 0.04$ (colder orbits; top row) and $J_R > 0.04$ (hotter orbits; bottom row). The left, middle, and right columns show the phase space color-coded with ΔN, V_R, and V_ϕ, respectively.

To acknowledge the fact that the perturbation happened in the past, and we observe the stars in the solar neighborhood at present, we retroactively tracked the orbits to make sure their present locations are indeed near the solar radius. Initially, all test particles are distributed around $R = 8.34$ kpc with median $V_\phi = 280\,\mathrm{km\,s^{-1}}$ ($\sigma_\phi = 15\ \mathrm{km\,s^{-1}}$) and median $V_R = 0\,\mathrm{km\,s^{-1}}$ ($\sigma_R = 20\ \mathrm{km\,s^{-1}}$), representing arches A1 and A2 at higher V_ϕ. Then the particle orbits are integrated backward without vertical perturbation ($V_Z = 0$, $Z = 0$). The distributions of the test particles in the $X - Y$ plane at 300 Myr ago are shown in panel (a1) of Figure 10. Then we impose the vertical perturbation on all the particles in two approaches.

The first approach is similar to Antoja et al. (2018), where the test particles are displaced vertically (median $Z = -0.3$ kpc and $V_Z = 0\,\mathrm{km\,s^{-1}}$ with dispersions of 0.2 kpc and $2\,\mathrm{km\,s^{-1}}$). For the 300 Myr case, after the perturbation, the $Z - V_Z$ phase space distribution is shown in panel (a3) of Figure 10. After 300 Myr of evolution, almost all the test particles now arrive in the solar radius, as shown in panel (a2) in the $X - Y$ plane, with a snail shell feature in the number density contrast map (ΔN) of the $Z - V_Z$ phase space distribution in panel (a4). In addition, we impose the same vertical perturbation on test particles at 400, 500, 600, and 700 Myr ago. The number density contrast maps (ΔN) of the final $Z - V_Z$ phase space distributions of the four tests are shown in Panels (b1)–(b4) in Figure 10.

In the second approach, under the impulsive approximation of the external perturbation (Binney & Schönrich 2018), a vertical velocity kick is imposed on all the test particles with the vertical positions barely changed (median $Z = 0$ and $V_Z = -10\,\mathrm{km\,s^{-1}}$ with a dispersion of 0.02 kpc and $10\,\mathrm{km\,s^{-1}}$). Panels (a1)–(a4) and (b1)–(b4) in Figure 11 show the test particle simulation results. Combining Figures 10 and 11, the snail shell becomes blurred or indistinct if the perturbation was imposed at least ∼500 Myr ago.

For comparison, we perform similar test particle simulations on colder orbits in arch A4 (Sirius). The test results are shown in Figure 12. Clearly, the snail becomes more tightly wound with the perturbation imposed at earlier stages. Compared to the snail shell shape in Figure 2 for the colder orbits, test particle simulations with perturbations imposed ∼500–600 Myr ago seem to agree well with the snail shell shape displayed by the colder orbits in Figure 2.

The test particle simulations support our conclusions about the faster phase-mixing of the hotter orbits. It seems that the vertical phase-mixing should have started at least 500 Myr ago, or there is not enough time for the snail shell pattern in hotter orbits to phase-mix away. Our result helps put tighter constraints on the vertical perturbation event of the Milky Way disk, which was suggested to occur ∼300–900 Myr ago (Antoja et al. 2018). The lack of a snail shell pattern can offer a new perspective, and can place important constraints on the occurrence time of the phase-mixing event.

Clearly, these test particle simulations still have limitations. For example, Darling & Widrow (2019) found that the phase space snail becomes less wound in a self-consistent simulation with self-gravity than the test particle run at longer timescales (∼1 Gyr). In the future more self-consistent simulations are desired to better constrain the detailed perturbation history of the Galactic disk.

We have shown that the existence or lack of prominent phase space snail shells is connected to the dichotomy of colder and hotter orbits, and to the different arches in the $V_R - V_\phi$ phase space. Our results and explanations strongly argue against the suggestion that the phase space snail shell is only produced by the major moving groups with no evidence of the ongoing vertical phase-mixing (Michtchenko et al. 2019). There are two obvious counterarguments to their suggestion. First, arches A3 and A6, which do not contain any of the major moving groups, still show a phase space snail shell. Second, the Hercules slow branch (A9), despite being a major moving group, shows no prominent snail shell feature.

3.4. V_R and V_ϕ Color-coded Phase Spaces

Binney & Schönrich (2018) suggested that the vertical and radial oscillation frequencies (Ω_Z, Ω_R) anti-correlate with V_ϕ (hence the angular momentum or the guiding radius R_g). Stars with different V_ϕ follow a narrow and sequential trend in the $\Omega_Z - \sqrt{J_Z}$ plane, leading to the formation of the snail shell in the V_ϕ color-coded phase space. On the other hand, faster Ω_R leads to a faster change of V_R. Therefore, the V_R color-coded phase space shears into a spiral that differs from the V_ϕ color-coded phase space spiral in the tightness of the winding (Binney & Schönrich 2018). Different simulations also indicate that the coupled motions in horizontal and vertical directions lead to clear snail shells in V_R and V_ϕ color-coded phase spaces (Darling & Widrow 2019; Laporte et al. 2019). In particular, the bar-buckling perturbation scenario predicts the most clear snail shell in V_R color-coded phase space (Khoperskov et al. 2019).

However, for some arches in colder orbits, V_R or V_ϕ color-coded phase spaces show no clear snail shell (see Figure 2). It may be understandable for arches with a narrow range of V_ϕ. For example, the V_ϕ range of arch A4 (Sirius) is only $15\,\mathrm{km\,s^{-1}}$, which makes it difficult to highlight snail shell (with larger ΔV_ϕ) in the V_ϕ color-coded phase space. In Figure 6, if we combine all the stars on colder orbits, a moderate snail shell in V_ϕ (and even weaker in V_R) color-coded phase space is present. These results suggest that the coupling between the in-plane and vertical motions may be weaker for the colder orbits than previously expected.

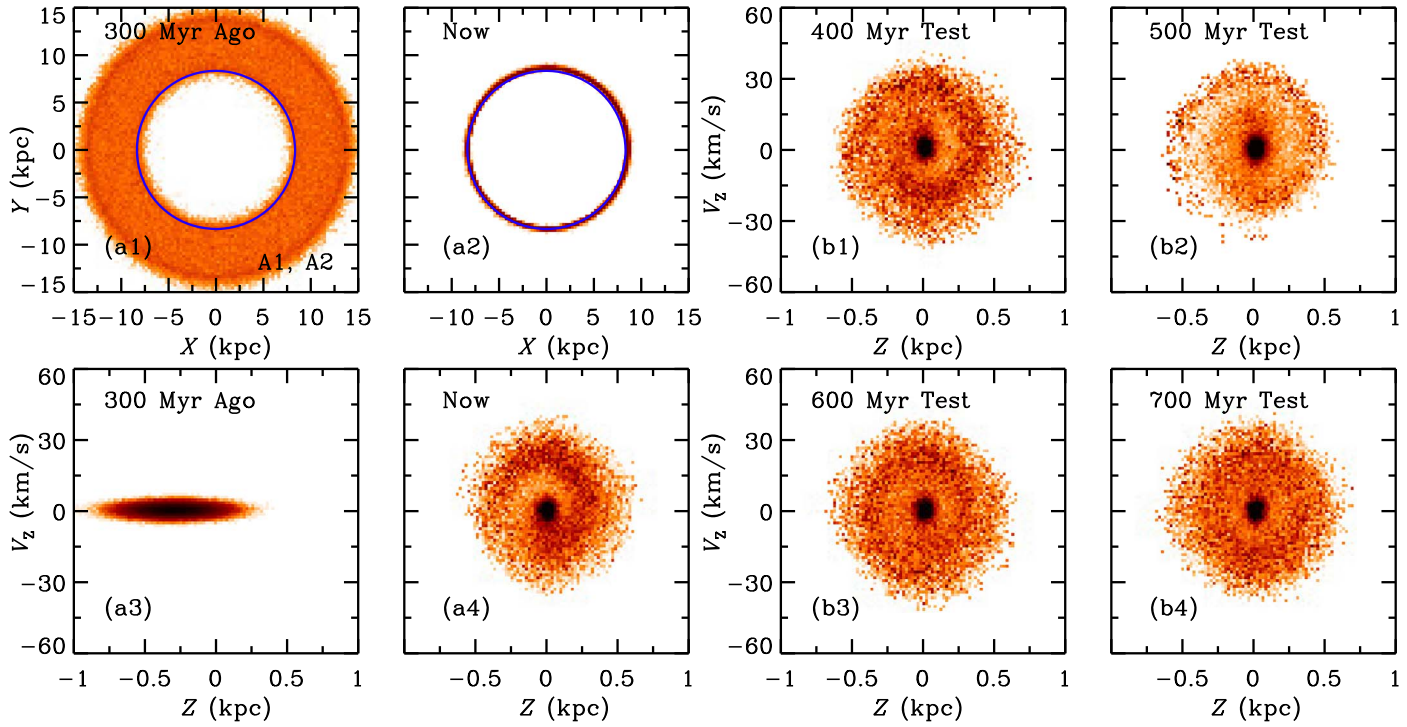

Figure 10. Test particle simulation of the first approach showing the phase-mixing of stars on hotter orbits in arches A1 and A2. Panels (a1)–(a4) show the simulation results with the vertical perturbation imposed 300 Myr ago. Panels (a1) and (a2) show the face-on distribution of the test particles 300 Myr ago and now, with the blue circle representing the solar radius ($R = 8.34$ kpc). Panels (a3) and (a4) are the corresponding number density contrast maps of the $Z - V_Z$ phase space. Other test results with the vertical perturbation imposed on the test particle simulations at 400, 500, 600, and 700 Myr ago are shown in panels (b1)–(b4).

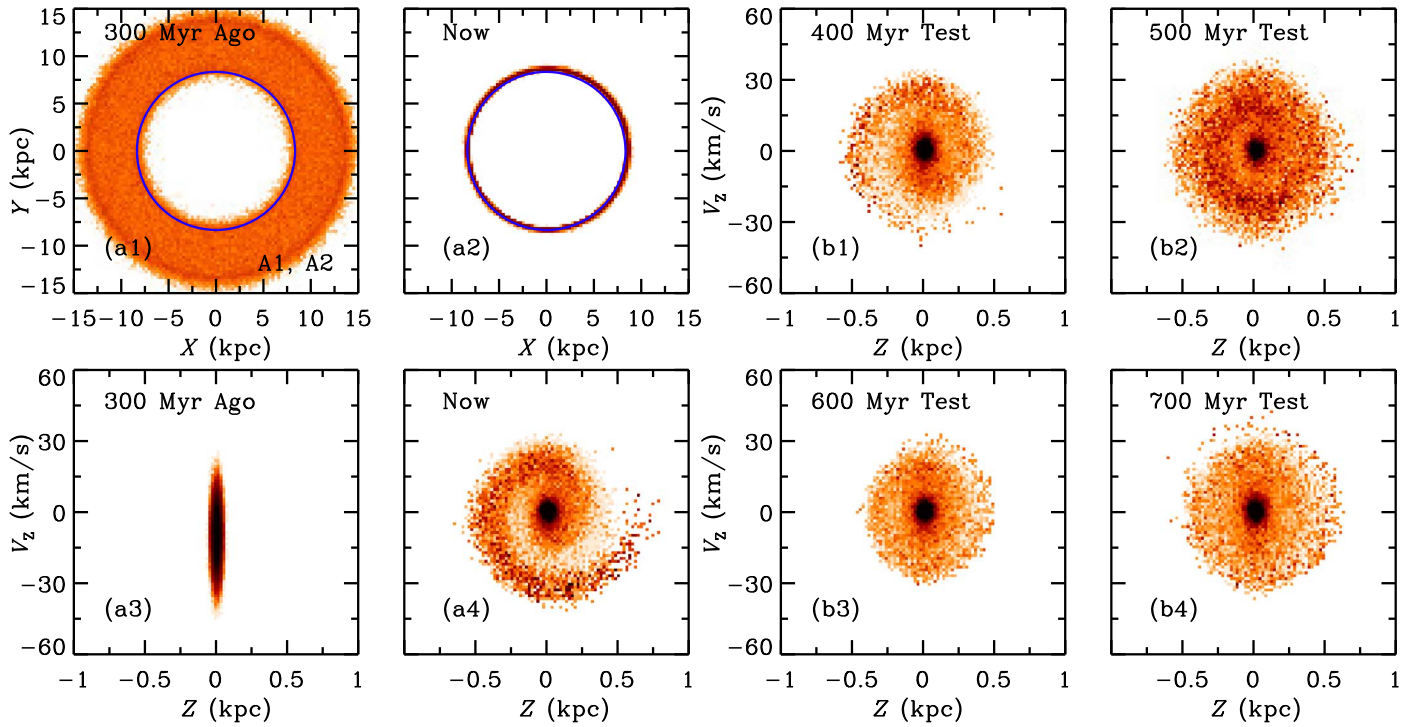

Figure 11. Test particle simulation of the second approach showing the phase-mixing of stars on hotter orbits in arches A1 and A2. The layout here mirrors that of Figure 10.

3.5. The Enhanced Snail Shell in V_ϕ Color-coded Phase Space

Mathematically speaking, the V_ϕ color-coded phase space in Antoja et al. (2018) is just the number-weighted average of the azimuthal velocity of all the arches. In an ideal case, imagine that there is only one arch at some V_ϕ and a featureless background at lower V_ϕ. If all the stars in this arch are arranged

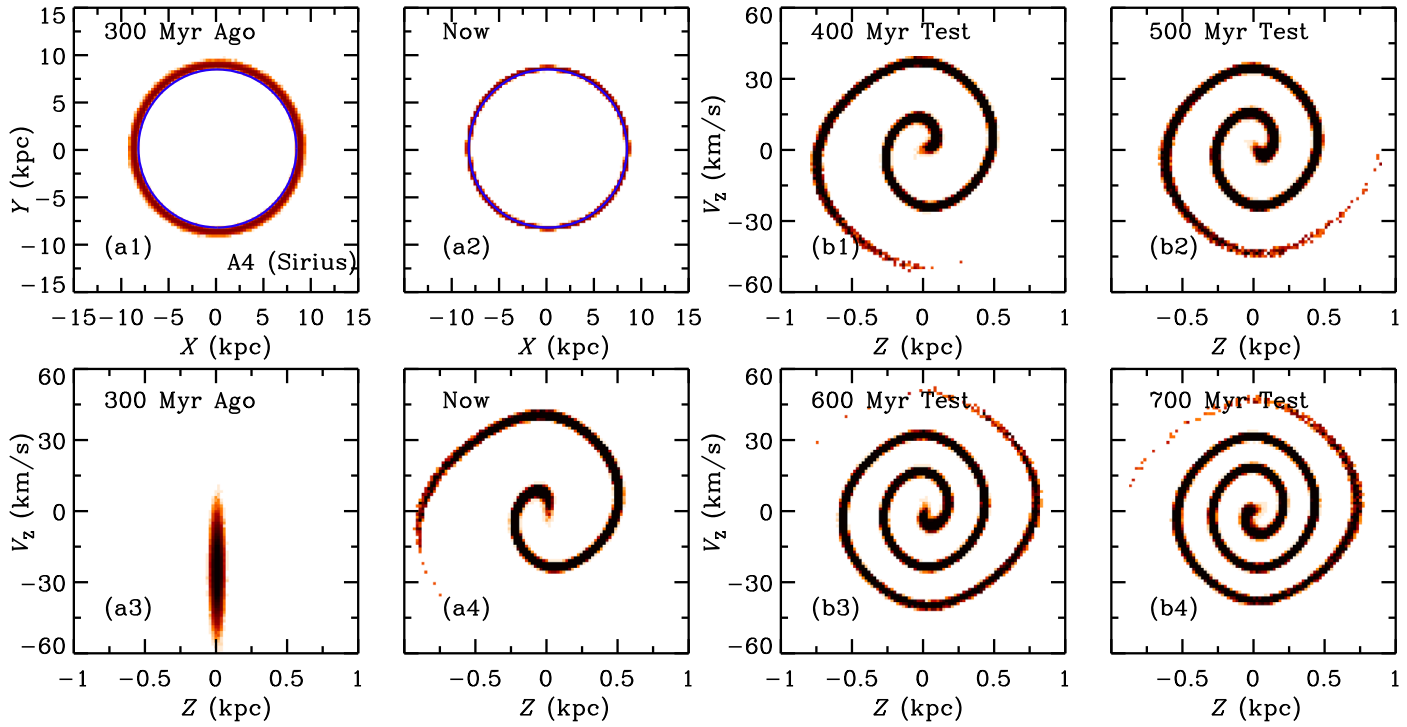

Figure 12. Test particle simulation of the second approach showing the phase-mixing of stars on colder orbits in arch A4 (Sirius). The layout here mirrors that of Figure 10. The snail shell is more tightly wound for the earlier perturbations.

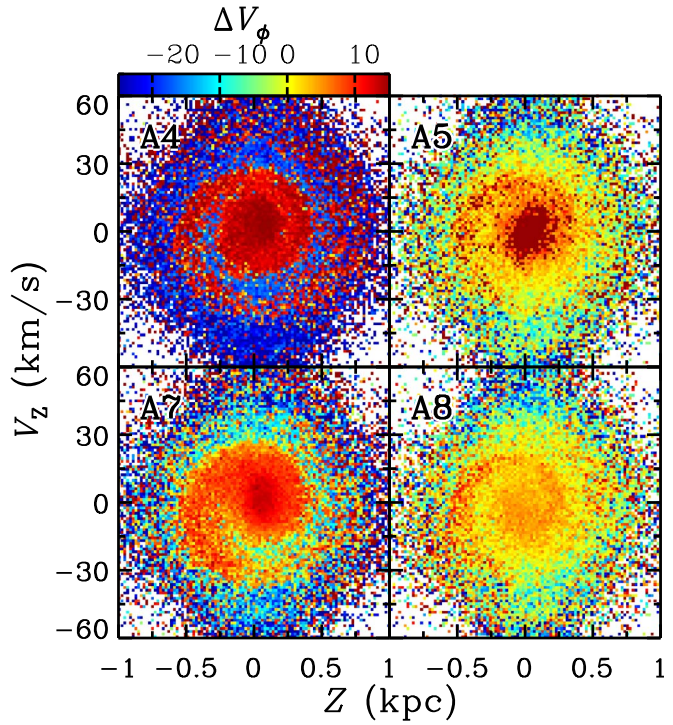

Figure 13. V_ϕ color-coded $Z - V_Z$ phase space of the arches in Figure 2 showing a clear snail shell combined with the arches on hotter orbits in Figure 4 with a relatively smooth phase space distribution. The snail shell is prominent in the V_ϕ color-coded phase space after the combination, which is reminiscent of the shape in the number density phase space of each arch.

into a snail shell shape in $Z - V_Z$ number density phase space, then the combination with the smooth background at lower V_ϕ naturally results in a pronounced snail shell color-coded in V_ϕ, which in principle has the same shape as the snail shell in the number density distribution.

To demonstrate this argument, we create a featureless background by combining all the stars on the hotter orbits.[9] The background is then combined with each arch on the colder orbits, namely, A4, A5, A7, and A8. Clear snail shells can be seen in the V_ϕ color-coded phase space of each composition shown in Figure 13. Consistent with our expectation, for each arch in Figure 13, the shape of the V_ϕ color-coded snail shell is consistent with the corresponding ΔN map as shown in Figure 2.

On the other hand, if we combine arches with different snail shell shapes at different V_ϕ, then the outcome color-coded with V_ϕ (or V_R) will be a snail shell slightly different from the number density map of the combination. To test this argument, we combine arches A4 and A7 together. The result is shown in Figure 14. Apparently, the number density contrast map and V_R and V_ϕ color-coded phase spaces show slightly different snail shell shapes, especially in the inner region of the phase space. This is mainly due to the different snail shell shapes between the two arches. From Figure 2, we can see that the shapes of the snail shells of the arches are not identical, especially in the central part of the phase space. Therefore, combining the arches in the colder orbits would result in different snail shell shapes between the number density map and the V_ϕ (or V_R) color-coded phase spaces, as shown in Figures 6 and 9. As shown in Figure 2, for each arch on colder orbits, the snail shell shapes are also different between the number density map and V_ϕ (or V_R) color-coded phase spaces, although the amplitude contrast of the snail shell is

[9] In order to highlight the V_ϕ color-coded snail shell in the Hercules Fast branch, arches A1 and A2 at higher V_ϕ are excluded from the hotter orbit background construction. The combination with those two arches will result in a less prominent, but still visible snail shell in the phase space when color-coded in V_ϕ.

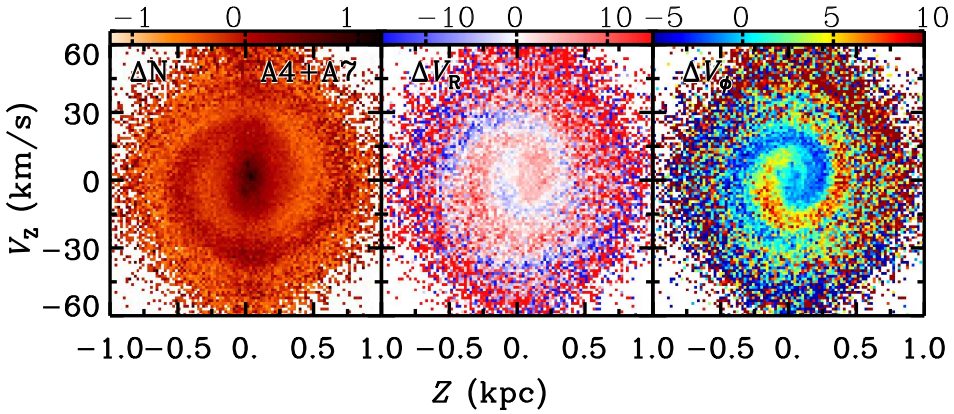

Figure 14. $Z - V_Z$ phase space distribution of the combination of arches A4 and A7. The left, middle, and right panels show the phase space color-coded with ΔN, V_R, and V_ϕ, respectively. Note that the snail shell in the ΔN map is different from that in the V_R or V_ϕ color-coded phase space.

only 2–4 km s^{-1}. This is probably due to the slight variation of the snail shell shape with V_ϕ (or V_R) for stars in each arch.

To summarize, it is the colder orbits that manifest the effect of ongoing vertical phase-mixing, with the hotter orbits providing a featureless background to highlight the snail shell of the colder orbits in the V_ϕ color-coded phase space. Moreover, combining the arches on colder orbits could result in different snail shell shapes color-coded in V_R or V_ϕ compared to the number density map.

4. Summary

We provide a new perspective for understanding the origin of the snail shell in the $Z - V_Z$ phase space and its dependence on the radial and azimuthal velocities with the *Gaia* DR2 data. We identify arches in the $V_R - V_\phi$ phase space, which include classical "moving groups" or "kinematic streams." Connections between the arches and the snail shell are investigated in detail. Interestingly, the snail shell only exists for stars on the colder orbits ($|V_\phi - V_{\rm LSR}| \lesssim 30$ km s^{-1}). Arches A3 (γLeo), A4 (Sirius), A5 (Coma), A6, A7 (Hyades–Pleiades), and A8 (Hercules Fast) all show prominent or moderate snail shell in the phase space number density distribution, but not for the arches A1, A2, A9 (Hercules Slow), A10, A11, and A12 (Arcturus), which are mainly composed of stars on hotter orbits.

The snail shell shapes are slightly different for the arches on the colder orbits. The amplitude of the snail shell is quantified by the difference between the local maximum and minimum of the ΔN profile along a narrow Z slit in the phase space. Consistent with the visual expectation, the amplitudes of the snail shell for the colder orbits ($\sim$0.3) are significantly higher than those for the hotter orbits ($\sim$0.03)

We use the radial action J_R to quantify the extent of the radial oscillation ("hotness") of orbits. The snail shell becomes much weaker for larger J_R values, and essentially disappears with $J_R > 0.04$. Thus, one should focus more on the colder orbits in future phase-mixing studies, with stars on the hotter orbits removed.

We also confirm that the Hercules stream is composed of two branches with different V_ϕ. Only the fast branch (A8) shows a prominent snail shell, but not the slow branch (A9). The Hercules stream may not be a homogeneous kinematic structure, which probably formed via different physical processes.

It seems that stars on hotter orbits have sufficiently phase-mixed to show significantly blurred and indistinct snail shells in $Z - V_Z$ space. The hotter orbits typically have much larger dynamical ranges in the disk than the colder orbits. Therefore, stars on hotter orbits make blurred elliptical rotation in the $Z - V_Z$ phase space, which leads to faster phase-mixing. These results help to put tighter constraints on the vertical perturbation history of the Milky Way disk. To explain the lack of a snail shell in the hotter orbits, the Milky Way disk should have been perturbed at least 500 Myr ago.

Khoperskov et al. (2019) proposed that during the buckling process, the bar can generate bending waves in the disk to form the phase space snail shell. The bar-buckling scenario predicts a more pronounced snail shell in the V_R color-coded phase space, rather than the V_ϕ or number-density color-coded phase space. However, this is not seen in our results. They also suggested that the snail shell can sustain for $\sim$4 Gyr due to the persistence of the bending wave in the disk. It is not clear if this scenario could explain the lack of snail shells in hotter orbits. In addition, the contribution of the bar-buckling mechanism on the Milky Way disk vertical perturbation may be much weaker compared to that of the Sagittarius dwarf (Laporte et al. 2019). Also this bar-buckling scenario may have some difficulty explaining recent observations on phase space distributions of different stellar populations (Tian et al. 2018; Laporte et al. 2019). Apparently, more theoretical efforts are needed in the future to better constrain the time of impact and to potentially determine the mass of the perturber. The coupling between the in-plane and vertical motions for the colder orbits may be weaker than previously thought.

The colder/hotter dichotomy in terms of the appearance of the phase space snail shell also provides a natural explanation for the significant snail shell in V_ϕ color-coded phase space. Since only the colder orbits exhibit the effect of ongoing vertical phase-mixing, the featureless phase space distribution of the hotter orbits provides a background to highlight the snail shell of the colder orbits in V_ϕ color-coded phase space. Moreover, combining the colder orbits together could result in different snail shell shapes in V_R or V_ϕ color-coded phase space compared to that in the number density map.

We thank the referee for helpful comments that improved the quality of the paper. We also want to thank Jerry Sellwood, Victor Debattista, Martin Smith, and Chao Liu for helpful suggestions and discussions. The research presented here is partially supported by the National Key R&D Program of China under grant No. 2018YFA0404501; by the National Natural

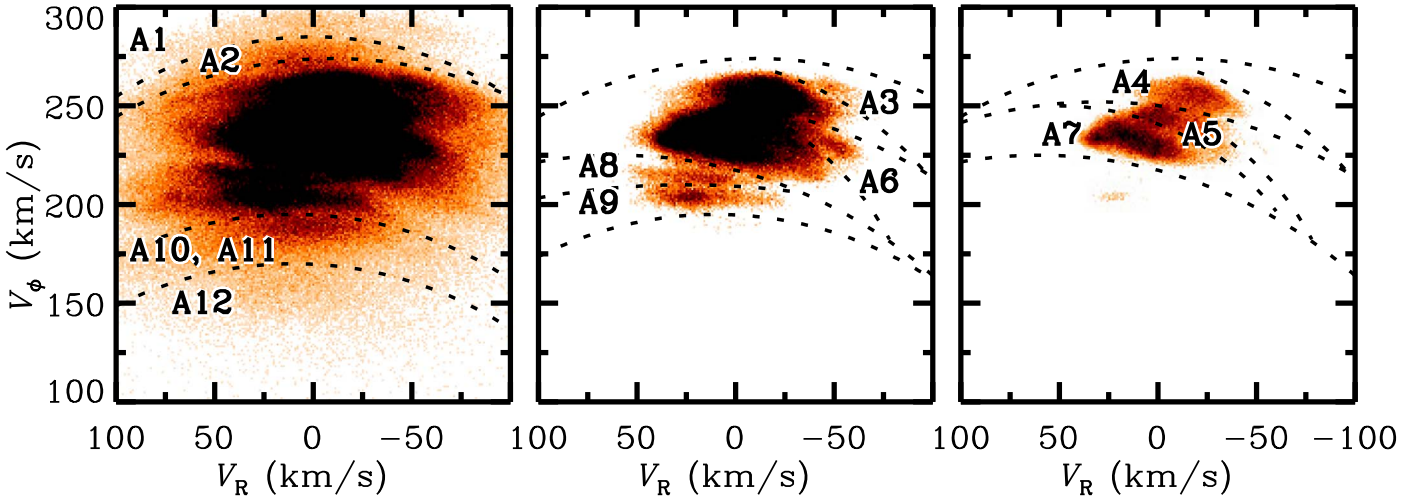

Figure 15. $V_R - V_\phi$ phase space distribution of the sample around $R = 8.34$ kpc. The three panels illustrate the identification of the gaps between the arches by changing the number density contrast levels, i.e., the minimum and maximum number densities to be displayed. Gaps at different number density levels can be much better visualized with different density contrast ranges.

Science Foundation of China under grants No. 11773052, 11761131016, and 11333003; and by the "111" Project of the Ministry of Education under grant No. B20019. Z.Y.L. is supported by the Youth Innovation Promotion Association, and the Key Lab of Computational Astrophysics, Chinese Academy of Sciences. J.S. acknowledges support from a *Newton Advanced Fellowship* awarded by the Royal Society and the Newton Fund. The paper was completed at KITP, which is supported in part by NSF grant PHY-1748958. This work made use of the facilities of the Center for High Performance Computing at Shanghai Astronomical Observatory.

This work has made use of data from the European Space Agency (ESA) mission *Gaia* (http://www.cosmos.esa.int/gaia), processed by the *Gaia* Data Processing and Analysis Consortium (DPAC, http://www.cosmos.esa.int/web/gaia/dpac/consortium). Funding for the DPAC has been provided by national institutions, in particular the institutions participating in the *Gaia* Multilateral Agreement.

Appendix
Arch Identification

The normalized empirical density distribution of the $V_R - V_\phi$ phase space is estimated with 1×1 $(\mathrm{km\,s^{-1}})^2$ bin size. With the wavelet transform method, Ramos et al. (2018) found the locations and extensions of the arches in $V_R - V_\phi$ space. To classify stars into different arches, it is necessary to determine the gaps between these arches identified in Ramos et al. (2018). Across the $V_R - V_\phi$ phase space, the stellar number density could vary by up to two orders of magnitude from one arch to another, as well as for the gaps between the different arches. In fact, gaps between arches with different number densities can be better visualized with different display contrasts, i.e., changing the minimum and maximum number densities to be shown in phase space. Figure 15 illustrates the $V_R - V_\phi$ phase space distribution of our sample with different number density contrasts. The left panel has the lowest number density threshold (between 1.0×10^{-6} and 6.2×10^{-5}), highlighting the arches with the lowest number density, i.e., A1, A2, A10, A11, and A12. Due to the ambient boundary between A10 and A11, they are grouped as a single arch in the analysis rather than separated. In the middle panel, the lower and upper number density thresholds are increased to 4.5×10^{-5} and 1.4×10^{-4}, respectively, leaving visible gaps at higher number densities. Arches A3, A6, A8, and A9 can be well separated. The right panel in Figure 15 highlights the three major arches in the highest-density region with a number density threshold between 1.0×10^{-4} and 3.0×10^{-4}, namely, A4 (Sirius), A5 (Coma), and A7 (Hyades and Pleiades).

ORCID iDs

Zhao-Yu Li https://orcid.org/0000-0001-5017-7021
Juntai Shen https://orcid.org/0000-0001-5604-1643

References

Antoja, T., Figueras, F., Fernández, D., & Torra, J. 2008, A&A, 490, 135
Antoja, T., Figueras, F., Romero-Gómez, M., et al. 2011, MNRAS, 418, 1423
Antoja, T., Helmi, A., Dehnen, W., et al. 2014, A&A, 563, A60
Antoja, T., Helmi, A., Romero-Gómez, M., et al. 2018, Natur, 561, 360
Antoja, T., Valenzuela, O., Pichardo, B., et al. 2009, ApJL, 700, L78
Bensby, T., Oey, M. S., Feltzing, S., & Gustafsson, B. 2007, ApJL, 655, L89
Binney, J., & Schönrich, R. 2018, MNRAS, 481, 1501
Binney, J., & Tremaine, S. 2008, Galactic Dynamics (2nd ed.; Princeton: Princeton Univ. Press)
Bland-Hawthorn, J., Sharma, S., Tepper-Garcia, T., et al. 2019, MNRAS, 486, 1167
Bovy, J. 2015, ApJS, 216, 29
Candlish, G. N., Smith, R., Fellhauer, M., et al. 2014, MNRAS, 437, 3702
Carlin, J. L., DeLaunay, J., Newberg, H. J., et al. 2013, ApJL, 777, L5
Chequers, M. H., & Widrow, L. M. 2017, MNRAS, 472, 2751
Darling, K., & Widrow, L. M. 2019, MNRAS, 484, 1050
de la Vega, A., Quillen, A. C., Carlin, J. L., Chakrabarti, S., & D'Onghia, E. 2015, MNRAS, 454, 933
Debattista, V. P. 2014, MNRAS, 443, L1
Dehnen, W. 1998, AJ, 115, 2384
Dehnen, W. 2000, AJ, 119, 800
D'Onghia, E., Madau, P., Vera-Ciro, C., Quillen, A., & Hernquist, L. 2016, ApJ, 823, 4
Famaey, B., Jorissen, A., Luri, X., et al. 2005, A&A, 430, 165
Faure, C., Siebert, A., & Famaey, B. 2014, MNRAS, 440, 2564
Friedli, D., Benz, W., & Kennicutt, R. 1994, ApJL, 430, L105
Fux, R. 2001, A&A, 373, 511
Gaia Collaboration, Brown, A. G. A., Vallenari, A., et al. 2018a, A&A, 616, A1
Gaia Collaboration, Katz, D., Antoja, T., et al. 2018b, A&A, 616, A2
Gómez, F. A., Minchev, I., O'Shea, B. W., et al. 2013, MNRAS, 429, 159
Gómez, F. A., Minchev, I., Villalobos, Á, O'Shea, B. W., & Williams, M. E. K. 2012, MNRAS, 419, 2163

Huang, Y., Liu, X.-W., Yuan, H.-B., et al. 2015, MNRAS, 449, 162
Hunt, J. A. S., & Bovy, J. 2018, MNRAS, 477, 3945
Hunter, C., & Toomre, A. 1969, ApJ, 155, 747
Irrgang, A., Wilcox, B., Tucker, E., & Schiefelbein, L. 2013, A&A, 549, A137
Kazantzidis, S., Bullock, J. S., Zentner, A. R., Kravtsov, A. V., & Moustakas, L. A. 2008, ApJ, 688, 254
Khoperskov, S., Di Matteo, P., Gerhard, O., et al. 2019, A&A, 622, L6
Laporte, C. F. P., Gómez, F. A., Besla, G., Johnston, K. V., & Garavito-Camargo, N. 2018a, MNRAS, 473, 1218
Laporte, C. F. P., Johnston, K. V., Gómez, F. A., Garavito-Camargo, N., & Besla, G. 2018b, MNRAS, 481, 286
Laporte, C. F. P., Minchev, I., Johnston, K. V., & Gómez, F. A. 2019, MNRAS, 485, 3134
Luri, X., Brown, A. G. A., Sarro, L. M., et al. 2018, A&A, 616, A9
McMillan, P. J. 2011, MNRAS, 414, 2446
Michtchenko, T. A., Barros, D. A., Pérez-Villegas, A., & Lépine, J. R. D. 2019, ApJ, 876, 36
Minchev, I., & Famaey, B. 2010, ApJ, 722, 112
Minchev, I., Quillen, A. C., Williams, M., et al. 2009, MNRAS, 396, L56
Monari, G., Famaey, B., & Siebert, A. 2015, MNRAS, 452, 747
Monari, G., Famaey, B., Siebert, A., et al. 2016, MNRAS, 461, 3835
Pérez-Villegas, A., Portail, M., Wegg, C., & Gerhard, O. 2017, ApJL, 840, L2
Purcell, C. W., Bullock, J. S., Tollerud, E. J., Rocha, M., & Chakrabarti, S. 2011, Natur, 477, 301
Quillen, A. C., Dougherty, J., Bagley, M. B., Minchev, I., & Comparetta, J. 2011, MNRAS, 417, 762
Quillen, A. C., Minchev, I., Bland-Hawthorn, J., & Haywood, M. 2009, MNRAS, 397, 1599
Quinn, P. J., Hernquist, L., & Fullagar, D. P. 1993, ApJ, 403, 74
Ramos, P., Antoja, T., & Figueras, F. 2018, A&A, 619, A72
Reid, M. J., Menten, K. M., Brunthaler, A., et al. 2014, ApJ, 783, 130
Roškar, R., Debattista, V. P., Quinn, T. R., Stinson, G. S., & Wadsley, J. 2008, ApJL, 684, L79
Schönrich, R. 2012, MNRAS, 427, 274
Schönrich, R., & Aumer, M. 2017, MNRAS, 472, 3979
Schönrich, R., McMillan, P., & Eyer, L. 2019, MNRAS, 487, 3568
Sellwood, J. A., & Binney, J. J. 2002, MNRAS, 336, 785
Siebert, A., Famaey, B., Binney, J., et al. 2012, MNRAS, 425, 2335
Siebert, A., Famaey, B., Minchev, I., et al. 2011, MNRAS, 412, 2026
Skuljan, J., Hearnshaw, J. B., & Cottrell, P. L. 1999, MNRAS, 308, 731
Starck, J.-L., & Murtagh, F. 2002, Astronomical Image and Data Analysis (Berlin: Springer)
Sun, N.-C., Liu, X.-W., Huang, Y., et al. 2015, RAA, 15, 1342
Tian, H.-J., Gupta, P., Sesar, B., et al. 2017, ApJS, 232, 4
Tian, H.-J., Liu, C., Carlin, J. L., et al. 2015, ApJ, 809, 145
Tian, H.-J., Liu, C., Wu, Y., Xiang, M.-S., & Zhang, Y. 2018, ApJL, 865, L19
Tremaine, S. 1999, MNRAS, 307, 877
Vasiliev, E. 2019, MNRAS, 482, 1525
Wang, C., Huang, Y., Yuan, H. B., et al. 2019, ApJL, 877, L7
Wang, H., Liu, C., Xu, Y., Wan, J.-C., & Deng, L. 2018b, MNRAS, 478, 3367
Wang, H., López-Corredoira, M., Carlin, J. L., & Deng, L. 2018a, MNRAS, 477, 2858
Widrow, L. M., Barber, J., Chequers, M. H., & Cheng, E. 2014, MNRAS, 440, 1971
Widrow, L. M., Gardner, S., Yanny, B., Dodelson, S., & Chen, H.-Y. 2012, ApJL, 750, L41